nature

https://doi.org/10.1038/s41586-026-10771-6

Accelerated Article Preview

Isotopic evidence for a cold and distant origin of 3I/ATLAS

Received: 20 February 2026

Accepted: 5 June 2026

Accelerated Article Preview
Published online: 22 June 2026

Cite this article as: Cordiner, M. et al. Isotopic evidence for a cold and distant origin of 3I/ATLAS. *Nature* https://doi.org/10.1038/s41586-026-10771-6 (2026)

Martin Cordiner, Nathan X. Roth, Marco Micheli, Geronimo Villanueva, Davide Farnocchia, Steven Charnley, Nicolas Biver, Dominique Bockelée-Morvan, Dennis Bodewits, Colin Orion Chandler, Jacques Crovisier, Maria N. Drozdovskaya, Kenji Furuya, Michael S. P. Kelley, Stefanie Milam, John W. Noonan, Cyrielle Opitom, Megan E. Schwamb & Cristina A. Thomas

This is a PDF file of a peer-reviewed paper that has been accepted for publication. Although unedited, the content has been subjected to preliminary formatting. Nature is providing this early version of the typeset paper as a service to our authors and readers. The text and figures will undergo copyediting and a proof review before the paper is published in its final form. Please note that during the production process errors may be discovered which could affect the content, and all legal disclaimers apply.

ACCELERATED ARTICLE PREVIEW

Isotopic Evidence for a Cold and Distant Origin of 3I/ATLAS

Martin Cordiner[1,2*], Nathan X. Roth[1,3], Marco Micheli[4], Geronimo Villanueva[1], Davide Farnocchia[5], Steven Charnley[1], Nicolas Biver[6], Dominique Bockelée-Morvan[6], Dennis Bodewits[7], Colin Orion Chandler[8,9,10], Jacques Crovisier[6], Maria N. Drozdovskaya[11,12], Kenji Furuya[13], Michael S. P. Kelley[14], Stefanie Milam[1], John W. Noonan[7], Cyrielle Opitom[15], Megan E. Schwamb[16], Cristina A. Thomas[10]

[1*]Solar System Exploration Division, NASA Goddard Space Flight Center, 8800 Greenbelt Road, Greenbelt, MD 20771, USA.
[2]Department of Physics, Catholic University of America, 620 Michigan Ave. NE, Washington, DC 20064, USA.
[3]Department of Physics, American University, 4400 Massachusetts Ave. NW, Washington, DC 20016, USA.
[4]ESA NEO Coordination Centre, Planetary Defence Office, European Space Agency, Largo Galileo Galilei, 1, 00044, Frascati, RM, Italy.
[5]Jet Propulsion Laboratory, California Institute of Technology, 4800 Oak Grove Dr., Pasadena, CA 91109, USA.
[6]LIRA, Observatoire de Paris, Université PSL, CNRS, Sorbonne Université, Université Paris Cité, CY Cergy Paris Université, 5 place Jules Janssen, F-92190 Meudon, France.
[7]Department of Physics, Auburn University, Edmund C. Leach Science Center, 36849, Auburn, AL, USA.
[8]DiRAC Institute, Department of Astronomy, University of Washington, 3910 15th Ave NE, Seattle, WA 98195, USA.
[9]LSST Interdisciplinary Network for Collaboration and Computing, 933 N. Cherry Avenue, Tucson, AZ 85721, USA.
[10]Department of Astronomy and Planetary Science, Northern Arizona University, PO Box 6010, Flagstaff, AZ 86011, USA.

ACCELERATED ARTICLE PREVIEW

[11]Physikalisch-Meteorologisches Observatorium Davos und Weltstrahlungszentrum (PMOD/WRC), Dorfstrasse 33, 7260 Davos Dorf, Switzerland.
[12]Department of Chemistry, Biochemistry and Pharmaceutical Sciences (DCBP), Universität Bern Freiestrasse 3, 3012 Bern, Switzerland.
[13]Pioneering Research Institute, RIKEN, 2-1 Hirosawa, Wako-shi, Saitama, 351-0198, Japan.
[14]Department of Astronomy, University of Maryland, 4296 Stadium Dr., PSC Bldg. 415, 20742-2421, College Park, MD, USA.
[15]Institute for Astronomy, University of Edinburgh, Royal Observatory, Edinburgh EH9 3HJ, UK.
[16]Astrophysics Research Centre, School of Mathematics and Physics, Queen's University Belfast, Belfast BT7 1NN, UK.

*Corresponding author(s). E-mail(s): martin.cordiner@nasa.gov;

Abstract

Interstellar objects provide the only directly observable samples of icy planetesimals formed around other stars, and can therefore provide insight into the diversity of physical and chemical conditions occurring during exoplanet formation [1–3]. Here we report isotopic measurements of the interstellar comet 3I/ATLAS, which reveal an elemental composition unlike any Solar System body. The water in 3I/ATLAS is enriched in deuterium, at a level of D/H = (0.98 ± 0.06)%, which is more than an order of magnitude higher than in known comets, while its range of $^{12}C/^{13}C$ ratios (141–191 for CO_2 and 123–172 for CO) exceeds typical values found in the Solar System, as well as nearby interstellar clouds and protoplanetary disks. Such extreme isotopic signatures indicate formation at temperatures $\lesssim$ 30 K in a relatively metal-poor environment. When interpreted with respect to models for Galactic chemical evolution, the carbon isotopic composition implies that 3I/ATLAS may have accreted as long ago as 12 billion years, following a period of intense, early star formation. 3I/ATLAS thus represents a preserved fragment of an ancient planetary system.

Keywords: Comets: 3I/ATLAS; Interstellar Objects; Infrared Spectroscopy; Composition; Isotopic Ratios; Galactic Chemical Evolution

3I/ATLAS is the third confirmed interstellar object to pass through our inner Solar System [4]. It exhibited surprisingly high gas production rates around perihelion, which have enabled detailed spectroscopic investigations [3, 5–7]. However, its exact time and place of origin, and the history of its path through the Galaxy, remain highly uncertain [8–10]. A broad range of ages (3–11) Gyr was deduced based on its high velocity, but

ACCELERATED ARTICLE PREVIEW

tracing the orbital trajectory back more than ~ 10 Myr is difficult due to unpredictable (chaotic) gravitational interactions within the inhomogeneous Galactic environment [11]. Isotopic ratio measurements provide invaluable insights into the physical and chemical conditions where 3I/ATLAS formed [12]: the D/H ratio is sensitive to the temperature and radiation environment [13], while the $^{12}C/^{13}C$ ratio reveals the degree of heavy-element enrichment (metallicity), which helps constrain the location (in space and time) of its natal interstellar gas cloud [14].

1 JWST and ALMA Observations

We obtained infrared spectral imagery of 3I/ATLAS using the James Webb Space Telescope (JWST) during the outbound leg of its 2025 perihelion passage. We simultaneously targeted emission lines from gas-phase water, carbon dioxide, and carbon monoxide (major isotopologues), in addition to their respective (deuterium and ^{13}C-bearing) minor isotopologues, allowing the derivation of precise isotopic ratios. The 2.7 μm H_2O fundamental rovibrational bands were observed on 2025-Dec-22, with a subsequent, deeper integration covering H_2O (hot bands), HDO, CO_2, $^{13}CO_2$, CO and ^{13}CO between 3.6–5.0 μm on 2025-Dec-23 (see Methods for details). A summary of the observed molecular bands is given in Extended Data Table 1. For the purpose of measuring the coma expansion velocity, complementary, ground-based submillimeter-wave observations of 3I/ATLAS's CO and HCN emission were obtained using the Atacama Compact Array (ACA — a subsystem of the Atacama Large Millimeter/submillimeter Array, ALMA) on 2025-Dec-22 (see Methods). 3I/ATLAS was at a heliocentric distance $r_H \approx 2.4$ au for all observations.

Multiple spectral lines from each of the major isotopologues were detected across the entirety of the NIRSpec field of view, confirming the presence of a spatially extended gas coma, with a peak intensity at the assumed position of the nucleus (the pseudo-nucleus). The image cubes for the major isotopologues were baseline-subtracted using a polynomial fit to the surrounding continuum regions in each pixel, then spectrally integrated to produce the molecular emission maps shown in Fig. 1. Spatially-integrated spectra (within a $d = 3.6''$-diameter circular aperture centered on the pseudo-nucleus) are shown for all the species of interest in Fig. 2.

Gas production rates (Q), rotational temperatures (T_{rot}), and isotopic ratios were derived by modelling the observed infrared emission lines as a function of sky-projected nucleocentric distance (ρ) using the Planetary Spectrum Generator (PSG [15]) (see Methods). The resulting Q_ρ curves for CO_2 and CO (Extended Data Fig. 1) reach a clear asymptote ("terminal" Q value) at $\rho \sim 0.3''$ ($\sim$ 400 km), indicating a lack of significant gas production for these species at larger radii, consistent with the majority of their outgassing arising directly from the nucleus. H_2O shows a significant increase in Q_ρ between $\rho \sim 0.3''$–$1.7''$ ($\sim$ 500–2,200 km), consistent with a contribution to the H_2O gas production from icy grain sublimation in the coma; uniformity of the HDO/H_2O ratio with radius (within the errors) implies similar gas release mechanisms for both H_2O and HDO.

Terminal gas production rates (Q_t) were calculated for each species from the average of the Q_ρ values in the 5 outermost annuli shown in Extended Data Fig. 1, and

ACCELERATED ARTICLE PREVIEW

are given in Extended Data Table 1. From these production rates, we find the following mixing ratios (and 1σ statistical uncertainties) for the main coma gas constituents within the JWST field of view: $CO_2/H_2O = 1.08 \pm 0.03$; $CO/H_2O = 2.40 \pm 0.07$; $CO/CO_2 = 2.24 \pm 0.01$. Since the earlier 2025-Aug-06 JWST observations [5] (obtained at $r_H = 3.32$ au inbound), the coma CO_2/H_2O ratio has fallen by a factor of ≈ 7, while the CO/H_2O and CO/CO_2 ratios have increased by factors of ≈ 1.4 and ≈ 10, respectively. This corresponds to a transition from a CO_2-dominated to a CO-dominated coma during the object's passage past the Sun (bracketing a likely H_2O-dominated phase around perihelion [6]), indicating a remarkable temporal evolution of the relative outgassing rates for these coma gases.

From the simultaneously-measured Q_t(HDO) and $Q_t(H_2O)$ values (see Methods), we derive a D/H mixing ratio for water of $(0.98 \pm 0.06)\%$. Spectral baseline definition is more challenging for $^{13}CO_2$ and ^{13}CO than HDO, so for those species we report the results considering an ensemble of best-fitting Q_t values across a range of plausible baseline models (the associated data are given in Extended Data Tables 2 and 3), resulting in $^{12}C/^{13}C = 141$–191 for CO_2 and 123–172 for CO. These ranges include the (additive) statistical $^{12}C/^{13}C$ uncertainties of 2% for CO_2 and 8% for CO, and should therefore be interpreted as the range of plausible fit parameters for each molecule.

2 Interpreting the Isotopic Ratios

The D/H and $^{12}C/^{13}C$ ratios for 3I/ATLAS are both extremely unusual among previously observed comets and other Solar System objects (Fig. 3). Although previous measurements of the $^{12}CO_2/^{13}CO_2$ ratio have been obtained in only two comets (67P and C/2017 K2), the $^{12}C/^{13}C$ ratio of the broader reservoir of volatile carbon in the Solar System (including other cometary gases), is well characterised. Observations of CH_4 in Jupiter, Saturn and Neptune, CO_2 on Mars and Venus, CH_4 ice on Eris and Makemake, as well as carbonates (and insoluble organic matter; IOM) in meteorites, and CN and C_2 in comets, all show remarkably similar $^{12}C/^{13}C$ ratios, consistent with terrestrial sedimentary rocks ($^{12}C/^{13}C = 89.4$), to within a few per cent, while the Solar ratio is 93.5 ± 0.7 [32]. The elevated $^{12}C/^{13}C$ ratios in 3I/ATLAS are therefore completely distinct from other materials measured in the Solar System, thus highlighting a non-local origin. The unusual isotopic ratios are supported by the findings of Salazar Manzano et al. [33] and Opitom et al. (manuscript submitted), who also found elevated D/H and $^{12}C/^{13}C$ ratios for 3I/ATLAS based on their respective ALMA and VLT observations (see Supplementary Discussion for further details).

Even outside the Solar System, measurements of $^{12}C/^{13}C > 100$ are rare, although such high ratios are predicted (and occasionally observed) in the outer parts of the Galaxy [14, 28, 29, 34]. The primary source of carbon in our Galaxy is from nucleosynthesis in the envelopes of asymptotic giant branch (AGB) stars, with additional, minor contributions from novae and supernovae [14, 35, 36]. Over their lifetimes, intermediate-mass AGB stars return material to the interstellar medium with increasingly-elevated elemental ^{13}C abundances, due to the conversion of ^{12}C to ^{13}C during hot bottom burning (*via* the CN cycle). Consequently, the cycle of star formation and death leads to increasing metallicity and decreasing $^{12}C/^{13}C$ ratios in

ACCELERATED ARTICLE PREVIEW

the interstellar medium as a function of Galactic age [14]. In particular regions where non-equilibrium chemistry can prevail, molecular $^{12}C/^{13}C$ ratios are subject to further modulation, as a result of isotope-selective photodissociation and low-temperature chemical kinetics [12, 37–39]. These processes can either deplete or enhance the $^{12}C/^{13}C$ ratios in hydrocarbons and nitriles, yet their impact on the $^{12}C/^{13}C$ ratio in CO — the main carbon reservoir in dense interstellar clouds — is typically small. The relative insensitivity of interstellar CO and CO_2 ice to isotopic fractionation processes at low temperatures contributes to the relative consistency of $^{12}C/^{13}C$ ratios across the Solar System. Consequently, the $^{12}C/^{13}C$ ratio in primitive planetary (and cometary) materials, including CO, CO_2 and their chemical derivatives, is thought to be close to the interstellar elemental value at the time of formation of the host star.

The elemental abundances observed in 3I/ATLAS place strict requirements on the chemical profile of its originating star-system, which, combined with dynamical constraints from the object's Galactic orbit (deduced from its inbound velocity vector), result in a set of criteria that help isolate its origin in space and time — see Supplementary Discussion (and Supplementary Table 1) for further details.

In a sample of 63 nearby solar-type stars, $^{12}C/^{13}C$ ratios were measured in the range 71–105 [40]. Based on their ages, which span $\sim$ 0–9 Gyr, a relatively rapid onset of ^{13}C enrichment was inferred, during the first 4 Gyr of our Galaxy's evolution, as a consequence of ^{13}C production in novae [41]. The resulting, steep $^{12}C/^{13}C$ curve at early times in their model with 3–8 $M_\odot$ white-dwarf nova progenitors (see Supplementary Figure 1), constrains the isotopic age of 3I/ATLAS to the range 11–12 Gyr, assuming an origin in the nearby Galactic disk. For comparison, the secondary $^{12}C/^{13}C$ peak at metallicity log_{10}[Fe/H] ≈ -0.5 in Fig. 19 of Kobayashi et al. [14] (thick-disk model), corresponds to a similarly old estimated age of $\sim$ 11 Gyr, even in the absence of ^{13}C production from novae.

Uncertainties in the modelled $^{12}C/^{13}C$ ratios as a function of time are significant due to incomplete knowledge of the stellar initial mass function, star formation rates as a function of time (and Galactocentric radius), interstellar gas infall/outflow rates and stellar nucleosynthetic yields. A conclusive age estimate for 3I/ATLAS is further complicated by the interstellar $^{12}C/^{13}C$ gradient as a function of Galactocentric distance [28, 29, 42] (see Supplementary Discussion). Ultimately, $^{12}C/^{13}C$ ratios within the range of plausible $^{12}C/^{13}C$ fit values for 3I/ATLAS can be most readily explained as a result of temporal evolution of the interstellar $^{12}C/^{13}C$ ratio, with a possible additional contribution from the Galactic radial $^{12}C/^{13}C$ gradient.

The D/H ratio for water in 3I/ATLAS demonstrates a surprisingly high deuterium enrichment compared with other (icy and non-icy) Solar System bodies and protostars within the Galaxy (Fig. 3a). The value of (0.98 ± 0.06)% lies 15σ above the mean D/H of 0.029% in Solar System comets (where σ is the combined standard deviation of the data), and 10σ above the mean water D/H of 0.1% found in the total sample of high and low-mass protostars. Within the Solar System, only Venus' atmosphere has a higher D/H, which results from mass-dependent atmospheric escape over the planet's lifetime [43]. By contrast, the deuteration of H_2O ice in Solar System comets is theorised to occur primarily in the interstellar and pre-stellar phases, where H_2O is rapidly synthesised on the surfaces of dust grains at very low temperatures ($\lesssim$

ACCELERATED ARTICLE PREVIEW

30 K) [44, 45]. Jensen et al. [13] showed that water deuteration occurs efficiently in star-forming regions as long as the dust temperatures remain below 20–30 K, while increased ultraviolet radiation fields and cosmic ray ionisation rates actually accelerate the reactions responsible for deuterating H_2O; a high D/H ratio $\sim 1\%$ is achieved in the presence of a cosmic ray flux $\gtrsim 10$ times the local Galactic value. Such enhanced-ionisation conditions would be expected in the vicinity of the lower-metallicity region of early, intense star-formation indicated by the high $^{12}C/^{13}C$ ratio and high abundances of C and O (α elements) in 3I/ATLAS. Several other properties of low-metallicity environments are theorised to accelerate the deuteration of H_2O ice, as summarised in the Supplementary Discussion.

A systematic difference is observed between the HDO/H_2O ratios in nearby protostellar envelopes and those found in Solar System comets (Fig. 3a). Although the number statistics are small for clustered and isolated protostars, the lower D/H ratios in clustered environments can be attributed to higher temperatures and a shorter, low-temperature protostellar collapse phase, that leads to inhibited D enrichment [13]. The D/H ratio in Solar System comets may have been further reduced by thermochemical reprocessing of water in the disk, as a consequence of radial mixing or sublimation and re-freezing, which incorporates re-equilibrated H_2O (with a lower D/H) back into the ice, thus lowering the bulk D/H ratio [46]. The exceptionally high D/H ratio measured in 3I/ATLAS therefore implies H_2O ice formation at very cold temperatures in an irradiated interstellar or protostellar environment, followed by a lack of significant, high-temperature reprocessing of its water in the disk. Although molecular ice and planetesimal formation is expected to be less efficient in reduced metallicity environments [47, 48], the HDO-rich composition of 3I/ATLAS proves that the cold, ice-rich conditions required for cometary accretion can still be maintained in less metal-rich (^{13}C-depleted) disks.

3 Conclusion

JWST observations of the interstellar comet 3I/ATLAS have revealed exceptionally high D/H and $^{12}C/^{13}C$ ratios in its coma. The observed elemental and isotopic abundance profile places strong constraints on the temperature and star-formation history of its originating environment. To obtain $D/H = 0.98\%$, the bulk of 3I/ATLAS's H_2O ice must have formed at temperatures $\lesssim 30$ K, with minimal contamination from water (re-)processed at higher temperatures. Its old, ^{13}C-poor natal environment was most likely embedded in a strongly-irradiated, interstellar cloud at relatively low metallicity, but enriched in C and O (and to lesser extents, N and S) in the aftermath of an intense period of massive star formation. Its distant origin in space and time makes 3I/ATLAS a uniquely-valuable tool for Galactic archaeology, highlighting the potential for interstellar object studies to help reveal the broader physical and chemical history of the Milky Way.

References

[1] Cordiner MA, Milam SN, Biver N, Bockelée-Morvan D, Roth NX, Bergin EA, et al. Unusually high CO abundance of the first active interstellar comet. Nature

ACCELERATED ARTICLE PREVIEW

Astronomy. 2020 Apr;4:861–866. https://doi.org/10.1038/s41550-020-1087-2. arXiv:2004.09586. [astro-ph.EP].

[2] Jewitt D, Seligman DZ. The Interstellar Interlopers. Annu. Rev. Astron. Astrophys.. 2023 Aug;61:197–236. https://doi.org/10.1146/annurev-astro-071221-054221. arXiv:2209.08182. [astro-ph.EP].

[3] Biver N, Bockelée-Morvan D, Moreno R, Crovisier J, Paubert G, Zakharov V, et al. Perihelion observations of interstellar comet 3I/ATLAS with the IRAM 30-m telescope. Astron. Astrophys.. 2026 Apr;708:L16. https://doi.org/10.1051/0004-6361/202659316.

[4] Seligman DZ, Micheli M, Farnocchia D, Denneau L, Noonan JW, Hsieh HH, et al. Discovery and Preliminary Characterization of a Third Interstellar Object: 3I/ATLAS. Astrophys. J. Lett.. 2025 Aug;989(2):L36. https://doi.org/10.3847/2041-8213/adf49a. arXiv:2507.02757. [astro-ph.EP].

[5] Cordiner MA, Roth NX, Kelley MSP, Bodewits D, Charnley SB, Drozdovskaya MN, et al. JWST Detection of a Carbon-dioxide-dominated Gas Coma Surrounding Interstellar Object 3I/ATLAS. Astrophys. J. Lett.. 2025 Oct;991(2):L43. https://doi.org/10.3847/2041-8213/ae0647. arXiv:2508.18209. [astro-ph.EP].

[6] Combi MR, Mäkinen T, Bertaux JL, Quémerais E, Ferron S, Lallement R, et al. Water Production of Interstellar Comet 3I/ATLAS from SOHO/SWAN Observations after Perihelion. Astrophys. J. Lett.. 2026 Feb;998(1):L17. https://doi.org/10.3847/2041-8213/ae3bd8.

[7] Kawakita H, Tsujimoto K, Shinnaka Y, Kobayashi H, Ootsubo T, Watanabe Ji. Postperihelion Optical Low-resolution Spectroscopy of Interstellar Comet 3I/ATLAS. The Astrophysical Journal Letters. 2026 mar;1000(2):L60. https://doi.org/10.3847/2041-8213/ae4c5b.

[8] Hopkins MJ, Dorsey RC, Forbes JC, Bannister MT, Lintott CJ, Leicester B. From a Different Star: 3I/ATLAS in the Context of the Ōtautahi–Oxford Interstellar Object Population Model. Astrophys. J. Lett.. 2025 Sep;990(2):L30. https://doi.org/10.3847/2041-8213/adfbf4. arXiv:2507.05318. [astro-ph.EP].

[9] Taylor AG, Seligman DZ. The Kinematic Age of 3I/ATLAS and Its Implications for Early Planet Formation. Astrophys. J. Lett.. 2025 Sep;990(1):L14. https://doi.org/10.3847/2041-8213/adfa28. arXiv:2507.08111. [astro-ph.EP].

[10] Guo Y, Zhang L, Feng F, Li ZY, Pomazan A, Yang X. Search for Past Stellar Encounters and the Origin of 3I/ATLAS. Astron. J.. 2025 Dec;170(6):362. https://doi.org/10.3847/1538-3881/ae1833. arXiv:2509.03361. [astro-ph.SR].

[11] Pérez-Couto X, Torres S, Villaver E, Mustill AJ, Manteiga M. 3I/ATLAS: In Search of the Witnesses to Its Voyage. arXiv e-prints.

ACCELERATED ARTICLE PREVIEW

2025 Sep;p. arXiv:2509.07678. https://doi.org/10.48550/arXiv.2509.07678. arXiv:2509.07678. [astro-ph.EP].

[12] Nomura H, Furuya K, Cordiner MA, Charnley SB, Alexander CMO, Nixon CA, et al. The Isotopic Links from Planet Forming Regions to the Solar System. In: Inutsuka S, Aikawa Y, Muto T, Tomida K, Tamura M, editors. Protostars and Planets VII. vol. 534 of Astronomical Society of the Pacific Conference Series; 2023. p. 1075.

[13] Jensen SS, Jørgensen JK, Furuya K, Haugbølle T, Aikawa Y. Modeling chemistry during star formation: water deuteration in dynamic star-forming regions. Astron. Astrophys.. 2021 May;649:A66. https://doi.org/10.1051/0004-6361/202040196. arXiv:2103.12135. [astro-ph.GA].

[14] Kobayashi C, Karakas AI, Umeda H. The evolution of isotope ratios in the Milky Way Galaxy. Mon. Not. R. Astron. Soc.. 2011 Jul;414(4):3231–3250. https://doi.org/10.1111/j.1365-2966.2011.18621.x. arXiv:1102.5312. [astro-ph.GA].

[15] Villanueva GL, Smith MD, Protopapa S, Faggi S, Mandell AM. Planetary Spectrum Generator: An accurate online radiative transfer suite for atmospheres, comets, small bodies and exoplanets. J. Quant. Spectrosc. Radiat. Transf.. 2018 Sep;217:86–104. https://doi.org/10.1016/j.jqsrt.2018.05.023. arXiv:1803.02008. [astro-ph.EP].

[16] Cordiner MA, Gibb EL, Kisiel Z, Roth NX, Biver N, Bockelée-Morvan D, et al. A D/H ratio consistent with Earth's water in Halley-type comet 12P from ALMA HDO mapping. Nature Astronomy. 2025 Aug;9:1476–1485. https://doi.org/10.1038/s41550-025-02614-7. arXiv:2508.05925. [astro-ph.EP].

[17] Tobin JJ, van't Hoff MLR, Leemker M, van Dishoeck EF, Paneque-Carreño T, Furuya K, et al. Deuterium-enriched water ties planet-forming disks to comets and protostars. Nature. 2023 Mar;615(7951):227–230. https://doi.org/10.1038/s41586-022-05676-z.

[18] Slavicinska K, van Dishoeck EF, Tychoniec Ł, Nazari P, Rubinstein AE, Gutermuth R, et al. JWST detections of amorphous and crystalline HDO ice toward massive protostars. Astron. Astrophys.. 2024 Aug;688:A29. https://doi.org/10.1051/0004-6361/202449785. arXiv:2404.15399. [astro-ph.SR].

[19] Slavicinska K, Tychoniec Ł, Navarro MG, van Dishoeck EF, Tobin JJ, van Gelder ML, et al. HDO Ice Detected toward an Isolated Low-mass Protostar with JWST. Astrophys. J. Lett.. 2025 Jun;986(2):L19. https://doi.org/10.3847/2041-8213/addb45. arXiv:2505.14686. [astro-ph.SR].

ACCELERATED ARTICLE PREVIEW

[20] Alexander CMOD, Fogel M, Yabuta H, Cody GD. The origin and evolution of chondrites recorded in the elemental and isotopic compositions of their macromolecular organic matter. Geochim. Cosmochim. Acta. 2007 Sep;71(17):4380–4403. https://doi.org/10.1016/j.gca.2007.06.052.

[21] Alexander CMOD, Newsome SD, Fogel ML, Nittler LR, Busemann H, Cody GD. Deuterium enrichments in chondritic macromolecular material—Implications for the origin and evolution of organics, water and asteroids. Geochim. Cosmochim. Acta. 2010 Aug;74(15):4417–4437. https://doi.org/10.1016/j.gca.2010.05.005.

[22] Alexander CMO, Bowden R, Fogel ML, Howard KT. Carbonate abundances and isotopic compositions in chondrites. Meteorit. Planet. Sci.. 2015 Apr;50(4):810–833. https://doi.org/10.1111/maps.12410.

[23] Yoshida TC, Nomura H, Furuya K, Tsukagoshi T, Lee S. A New Method for Direct Measurement of Isotopologue Ratios in Protoplanetary Disks: A Case Study of the ^{12}CO/^{13}CO Ratio in the TW Hya Disk. Astrophys. J.. 2022 Jun;932(2):126. https://doi.org/10.3847/1538-4357/ac6efb. arXiv:2204.08330. [astro-ph.EP].

[24] Qi C, Wilner DJ, Espaillat CC. Isotopic Ratios in the Disk of HD 163296. Astrophys. J. Lett.. 2026 Jan;997(1):L19. https://doi.org/10.3847/2041-8213/ae2916. arXiv:2601.02593. [astro-ph.EP].

[25] Brunken NGC, van Dishoeck EF, Slavicinska K, le Gouellec VJM, Rocha WRM, Francis L, et al. JOYS+ study of solid-state ^{12}C/^{13}C isotope ratios in protostellar envelopes: Observations of CO and CO_2 ice with the James Webb Space Telescope. Astron. Astrophys.. 2024 Dec;692:A163. https://doi.org/10.1051/0004-6361/202451794. arXiv:2409.17237. [astro-ph.SR].

[26] Smith RL, Pontoppidan KM, Young ED, Morris MR. HETEROGENEITY IN 12CO/13CO ABUNDANCE RATIOS TOWARD SOLAR-TYPE YOUNG STELLAR OBJECTS. The Astrophysical Journal. 2015 nov;813(2):120. https://doi.org/10.1088/0004-637X/813/2/120.

[27] Boogert ACA, Gerakines PA, Whittet DCB. Observations of the icy universe. Annu. Rev. Astron. Astrophys.. 2015 Aug;53:541–581. https://doi.org/10.1146/annurev-astro-082214-122348. arXiv:1501.05317. [astro-ph.GA].

[28] Luo G, Colzi L, Liu T, Bisbas TG, Li D, Sun Y, et al. A new measurement of the Galactic ^{12}C/^{13}C gradient from sensitive HCO^+ absorption observations. Astron. Astrophys.. 2024 Oct;690:A372. https://doi.org/10.1051/0004-6361/202451412. arXiv:2409.11821. [astro-ph.GA].

[29] Milam SN, Savage C, Brewster MA, Ziurys LM, Wyckoff S. The ^{12}C/^{13}C Isotope Gradient Derived from Millimeter Transitions of CN: The Case for Galactic Chemical Evolution. Astrophys. J.. 2005 Dec;634(2):1126–1132. https://doi.org/

ACCELERATED ARTICLE PREVIEW

10.1086/497123.

[30] Gandhi S, de Regt S, Snellen I, Zhang Y, Rugers B, van Leur N, et al. JWST Measurements of ^{13}C, ^{18}O, and ^{17}O in the Atmosphere of Super-Jupiter VHS 1256 b. Astrophys. J. Lett.. 2023 Nov;957(2):L36. https://doi.org/10.3847/2041-8213/ad07e2. arXiv:2311.05349. [astro-ph.EP].

[31] Crossfield IJM, Lothringer JD, Flores B, Mills EAC, Freedman R, Valverde J, et al. Unusual Isotopic Abundances in a Fully Convective Stellar Binary. Astrophys. J. Lett.. 2019 Jan;871(1):L3. https://doi.org/10.3847/2041-8213/aaf9b6. arXiv:1901.02607. [astro-ph.SR].

[32] Lyons JR, Gharib-Nezhad E, Ayres TR. A light carbon isotope composition for the Sun. Nature Communications. 2018 Mar;9:908. https://doi.org/10.1038/s41467-018-03093-3.

[33] Salazar Manzano LE, Paneque-Carreño T, Cordiner MA, Bergin EA, Lin HW, Lis DC, et al. Water D/H in 3I/ATLAS as a probe of formation conditions in another planetary system. Nature Astronomy. 2026 Apr;https://doi.org/10.1038/s41550-026-02850-5. arXiv:2603.07026. [astro-ph.EP].

[34] Romano D, Matteucci F, Zhang ZY, Papadopoulos PP, Ivison RJ. The evolution of CNO isotopes: a new window on cosmic star formation history and the stellar IMF in the age of ALMA. Mon. Not. R. Astron. Soc.. 2017 Sep;470(1):401–415. https://doi.org/10.1093/mnras/stx1197. arXiv:1704.06701. [astro-ph.GA].

[35] Romano D, Matteucci F. Nova nucleosynthesis and Galactic evolution of the CNO isotopes. Mon. Not. R. Astron. Soc.. 2003 Jun;342(1):185–198. https://doi.org/10.1046/j.1365-8711.2003.06526.x. arXiv:astro-ph/0302233. [astro-ph].

[36] Ramstedt S, Olofsson H. The ^{12}CO/^{13}CO ratio in AGB stars of different chemical type. Connection to the ^{12}C/^{13}C ratio and the evolution along the AGB. Astron. Astrophys.. 2014 Jun;566:A145. https://doi.org/10.1051/0004-6361/201423721. arXiv:1405.6404. [astro-ph.SR].

[37] Langer WD, Graedel TE, Frerking MA, Armentrout PB. Carbon and oxygen isotope fractionation in dense interstellar clouds. Astrophys. J.. 1984 Feb;277:581–604. https://doi.org/10.1086/161730.

[38] Visser R, van Dishoeck EF, Black JH. The photodissociation and chemistry of CO isotopologues: applications to interstellar clouds and circumstellar disks. Astron. Astrophys.. 2009 Aug;503(2):323–343. https://doi.org/10.1051/0004-6361/200912129. arXiv:0906.3699. [astro-ph.GA].

[39] Lee S, Nomura H, Furuya K. Carbon Isotope Chemistry in Protoplanetary Disks: Effects of C/O Ratios. Astrophys. J.. 2024 Jul;969(1):41. https://doi.org/10.3847/1538-4357/ad39e3. arXiv:2404.01635. [astro-ph.GA].

ACCELERATED ARTICLE PREVIEW

[40] Botelho RB, Milone AdC, Meléndez J, Alves-Brito A, Spina L, Bean JL. Carbon, isotopic ratio $^{12}C/^{13}C$, and nitrogen in solar twins: constraints for the chemical evolution of the local disc. Mon. Not. R. Astron. Soc.. 2020 Dec;499(2):2196–2213. https://doi.org/10.1093/mnras/staa2917. arXiv:2009.09003. [astro-ph.SR].

[41] Romano D. The evolution of CNO elements in galaxies. Astron. Astrophys. Rev.. 2022 Dec;30(1):7. https://doi.org/10.1007/s00159-022-00144-z. arXiv:2210.04350. [astro-ph.GA].

[42] Yan YT, Henkel C, Kobayashi C, Menten KM, Gong Y, Zhang JS, et al. Direct measurements of carbon and sulfur isotope ratios in the Milky Way. Astron. Astrophys.. 2023 Feb;670:A98. https://doi.org/10.1051/0004-6361/202244584. arXiv:2212.03252. [astro-ph.GA].

[43] Donahue TM, Hoffman JH, Hodges RR Jr, Watson AJ. Venus Was Wet: A Measurement of the Ratio of Deuterium to Hydrogen. Science. 1982;216(4546):630–633. https://doi.org/10.1126/science.216.4546.630.

[44] Taquet V, Charnley SB, Sipilä O. Multilayer Formation and Evaporation of Deuterated Ices in Prestellar and Protostellar Cores. Astrophys. J.. 2014 Aug;791(1):1. https://doi.org/10.1088/0004-637X/791/1/1. arXiv:1405.3268. [astro-ph.GA].

[45] Furuya K, Drozdovskaya MN, Visser R, van Dishoeck EF, Walsh C, Harsono D, et al. Water delivery from cores to disks: Deuteration as a probe of the prestellar inheritance of H_2O. Astron. Astrophys.. 2017 Mar;599:A40. https://doi.org/10.1051/0004-6361/201629269. arXiv:1610.07286. [astro-ph.GA].

[46] Jacquet E, Robert F. Water transport in protoplanetary disks and the hydrogen isotopic composition of chondrites. Icarus. 2013 Apr;223(2):722–732. https://doi.org/10.1016/j.icarus.2013.01.022. arXiv:1301.5665. [astro-ph.EP].

[47] Guadarrama R, Vorobyov EI, Rab C, Güdel M. The effect of metallicity on the abundances of molecules in protoplanetary disks. Astron. Astrophys.. 2022 Nov;667:A28. https://doi.org/10.1051/0004-6361/202140995. arXiv:2208.09327. [astro-ph.SR].

[48] Andama G, Mah J, Bitsch B. Which stars can form planets: Planetesimal formation at low metallicities. Astron. Astrophys.. 2024 Mar;683:A118. https://doi.org/10.1051/0004-6361/202348899. arXiv:2401.16155. [astro-ph.EP].

ACCELERATED ARTICLE PREVIEW

Methods

JWST Observations

Observations of 3I/ATLAS were performed using the JWST NIRSpec integral field unit (IFU) [49], as part of program ID 5094. The G235H dispersive element was used for a single 642 s exposure starting UT 2025-12-22 03:36, covering wavelengths $\lambda = 1.7$–3.2 μm, followed by 5×700 s exposures with the G395H disperser starting UT 2025-12-23 08:07, covering $\lambda = 2.9$–5.3 μm. The resulting 30×30 array of spectra have a resolving power $R_\lambda = \lambda/\Delta\lambda \sim 2700$ and a pixel size of $0.1''$, which is approximately the same as the FWHM of the JWST point-spread function at 3 μm.

3I/ATLAS was acquired and tracked in the IFU using JPL Horizons ephemeris solution #42. During observations, the object was 1.80 au from the telescope, at $r_H = 2.37$–2.42 au, with a (Sun-target-observer) phase angle of $22.7°$–$21.6°$. Each exposure was divided across four dither positions, spatially separated (in the approximate shape of a square) with offsets of $\approx 0.2''$ from the (central) targeted position. The data were reduced using the JWST Calibration Pipeline software version v1.20.2 [50] using the JWST Calibration Reference Data System context file 1464. The multiple dithers for each exposure were shifted and combined in the rest frame of the comet during image processing, thus allowing detector artifacts and cosmic ray events to be identified and removed. For each 3I/ATLAS exposure, a set of sky background exposures with matching exposure time, disperser and dither settings was obtained, offset by $300''$ from the science target, along the horizontal axis of the IFU aperture. Unfortunately, two of the five background exposures for G395H failed due to guide-star acquisition issues; these exposures will be re-observed later in 2026. Inspection of the available background exposures showed no evidence for significant emission from any background (*e.g.* interstellar) infrared sources or zodiacal light, so the final science data cubes were reduced without background subtraction in order to maximise the signal-to-noise ratio (SNR).

After centering on the comet, the individual exposures were combined and rebinned onto a common spatial-spectral coordinate system using the 3D drizzle algorithm included as part of the JWST pipeline's `cube_build` task [51]. The resulting image cube spatial dimensions were $\approx 3.7'' \times 3.5''$ for G235H and $\approx 4.4'' \times 4.0''$ for G395H. The absolute flux calibration accuracy of the final data cubes is expected to be 3%.[1].

To produce spectrally integrated emission maps, the observed data cubes in the vicinity of each emission band were first continuum-subtracted (pixel-by-pixel), using polynomial fits to the spectral baseline regions surrounding the detected emission lines. For H_2O, a 7th-order polynomial was used (fitted between 2.55–2.90 μm); for CO_2, 1st order was used (fitted between 4.188–4.500 μm, with the CO_2 ν_3 band masked between 4.20–4.44 μm); for CO, 4th order was used (fitted between 4.50–4.85 μm). Spectral line emission was excluded from the continuum fits using an iterative sigma-clipping algorithm with a rejection threshold 2.8 times the residual RMS. The detected line emission was then spectrally integrated to produce the maps in Fig. 1. Although the signal-to-noise ratio (SNR) per pixel was too low to allow useful mapping of the minor

[1] https://jwst-docs.stsci.edu/jwst-calibration-status/nirspec-calibration-status/nirspec-ifu-calibration-status

ACCELERATED ARTICLE PREVIEW

isotopologues (HDO and ^{13}CO), significant emission from these species is detected in larger extraction apertures (see Fig. 2).

Astrometry

In order to guarantee the acquisition of 3I/ATLAS within the small ($3'' \times 3''$) NIRSpec IFU field of view, while allowing for the $0.2''$ dither offsets and $0.1''$ telescope blind pointing accuracy, we had to ensure an ephemeris accuracy better than $\pm 1.2''$ (at 3σ confidence). To reach such a high accuracy, we performed astrometric measurements of 3I/ATLAS in the weeks leading up to our JWST observations using images contributed by observers at various professional telescope facilities, located at sites with good seeing conditions (see Acknowledgements for further details). These included the Canada-France-Hawai'i Telescope, Lowell Discovery Telescope, Apache Point Observatory (APO), Southern Astrophysical Research telescope, the Las Cumbres Observatory, and the University of Hawai'i 2.2 m telescope. Good seeing was essential to resolve the inner coma and the pseudo-nucleus with the greatest possible precision, ensuring a positional measurement as close as possible to the actual location of the cometary nucleus.

In the presence of asymmetric outgassing, the inner coma is often distorted in an antisolar direction, and most common astrometric centroiding procedures tend to become biased away from the nucleus and towards the tail. This issue was mitigated using the comet-specific, zero-aperture extrapolation method [52, 53]. Astrometry was reported to the Minor Planet Center, ensuring it would be available by the time of scheduling and properly included in the solution posted on the JPL Horizons database.

Spectral Modeling

Gas production rates (Q) and rotational temperatures (T_{rot}), were derived as a function of distance from the nucleus for H_2O, CO_2, and CO, using optimal estimation routines as part of the Planetary Spectrum Generator (PSG [15], based on synthetic fluorescence models described by Villanueva et al. [54]). To take advantage of the spatial information in our dataset, our modelling strategy followed a similar "Q-curve" formalism to that used by previous JWST cometary studies [5, 55]. Pixels close to the nucleus are affected by PSF-related flux losses and (for stronger lines), opacity effects, which are difficult to accurately model. We therefore derived gas production rates as a function of ρ within successive $0.2''$-wide annuli, centered on the brightest (pseudo-nucleus) pixel. Assuming uniform, isotropic gas production with a constant outflow velocity (v_{out}), the Q value converges to an asymptote, or terminal Q value (Q_t), at a characteristic ρ value, at which point the unmodelled flux losses are negligible and Q_t then represents the total molecular production rate within the field of view. To avoid contamination of these results by noisier pixels at the IFU edges, the Q curves were computed up to $\rho = 1.8''$, corresponding to the $3.6''$-diameter circular integration apertures used in Figure 2. The gas outflow velocity was set to 0.310 km s^{-1} for H_2O and CO_2, and 0.345 km s^{-1} for CO, based on contemporaneous observations of the spectrally resolved HCN and CO line shapes, using the ALMA Atacama Compact Array (see ALMA Observations section). Molecular photolysis rates appropriate

ACCELERATED ARTICLE PREVIEW

for the active Sun were incorporated from ref. [56]. The spectral resolution for each NIRSpec grating (as a function of wavelength) was taken from the dispersion curves available at https://jwst-docs.stsci.edu.

Statistical 1σ parameter uncertainties were derived from the diagonal elements of the fit covariance matrix, scaled according to the square root of the reduced chi-square (χ^2_R) to ensure the baseline noise level was realistically accounted for. For all species apart from CO_2 the spectral baseline shape (with contributions due to scattered sunlight and thermal emission from the coma dust and nucleus, combined in some cases with instrumental artifacts), was determined by fitting a polynomial function simultaneously with the gas emission lines. This way, statistical uncertainties in the baseline shape are propagated into the final uncertainties on each Q value. For CO_2, the inaccurate model fit to some of the higher-J CO_2 lines (possibly due to the presence of multiple T_{rot} components or non-LTE effects) results in the baseline fit becoming skewed in the direction of the fit residuals. Therefore, prior to performing the CO_2 Q-curve analysis, it was necessary to subtract a fitted linear baseline from these data pixel-by-pixel (with the CO_2 + $^{13}CO_2$ line-containing region masked between 4.20–4.44 μm). Due to the high CO_2 line-to-continuum ratio ($\sim$ 200), uncertainties in the baseline placement for this species have negligible impact on its retrieved production rate.

When fitting individual isotopologues, PSG reports total production rates summed over all isotopologues assuming terrestrial isotopic abundance ratios. Therefore, to obtain individual isotopologue Q values, it was necessary to multiply the PSG results by the terrestrial abundance fractions, given at https://hitran.org/docs/iso-meta/.

The H_2O band at 2.7 μm (in the G235H setting) contains multiple, high-SNR, spectrally resolved rovibrational lines of the ortho (o) and para (p) H_2O spin states (with H-atom spins parallel *vs.* antiparallel, respectively), so this band was used to determine $T_{rot}(H_2O)$ and the H_2O ortho-to-para ratio (OPR) — key parameters for reliably measuring $Q(H_2O)$ from the weaker, more blended 4.5–5.1 μm H_2O hot bands that were observed simultaneously with HDO in the G395H setting. We modelled o- and p-H_2O simultaneously, but as separate species, allowing Q(o-H_2O), Q(p-H_2O), and T_{rot} to vary as free parameters, and with a 7th order polynomial baseline. An example of the spectral fit quality is shown in Extended Data Fig. 4.

The terminal (asymptotic) p-H_2O production rate is $Q_t = (3.79 \pm 0.02) \times 10^{26}$ s^{-1}, while for o-H_2O, $Q_t = (1.04 \pm 0.01) \times 10^{27}$ s^{-1}, leading to OPR = 2.74 ± 0.03, with a total (terminal) water production rate $Q_t(H_2O) = (1.42 \pm 0.01) \times 10^{27}$ s^{-1}, summed over the ortho and para contributions. Due to the large o- and p-H_2O emission line strengths compared with the continuum around 2.7 μm, these results are not significantly dependent on the choice of baseline polynomial order. The 3I/ATLAS OPR is consistent with a spin temperature of $T_{spin} \approx 35$ K [57]. The fact that the associated H_2O rotational temperature of 14.5 ± 0.1 K is considerably smaller than the spin temperature, implies that the H_2O OPR is not being dictated by T_{rot}. Furthermore, constancy of the OPR as a function of radius indicates that it is not being significantly altered within the coma, and instead reflects conditions associated with the release of water from the nucleus.

ACCELERATED ARTICLE PREVIEW

The H_2O hot bands around 5 μm contained insufficient unblended lines for a reliable T_{rot} and OPR retrieval, but since they were observed simultaneously with HDO, the hot band lines were used to derive $Q_t(H_2O)$ for direct comparison with Q_t(HDO). For the H_2O hot band (and HDO), the OPR was fixed at 2.74 and the rotational temperature for each annulus ($T_{rot}(\rho)$) was held fixed according to the $T_{rot}(\rho)$ values previously derived from the H_2O 2.7 μm band. Many of the H_2O hot-band lines in our data are blended with lines from CO, CN and OCS, so to derive $Q(H_2O)$, we focused on the 4.5–4.7 μm region, which contains three of the stronger, unblended H_2O lines (see Fig. 2a). Prior to fitting the H_2O spectrum in each annulus, we subtracted the interloping CO lines, using a set of independent Gaussian fits, to facilitate identification of the spectral baseline. The spectral regions within the boundaries of each subtracted CO line (see Fig. 2a) were further masked to prevent any remaining CO line residuals from biasing the fit. The resulting $Q_\rho(H_2O)$ curve is shown in Extended Data Fig. 1a. Taking the average of the outer 5 annuli gives $Q_t(H_2O) = (1.64 \pm 0.05) \times 10^{27}$ s^{-1}, which is 15% larger than the value obtained from the G235H setting on the previous day, indicative of moderate temporal evolution in 3I/ATLAS's activity.

Four individual rovibrational lines of HDO were clearly detected, as part of the ν_1 band between $\lambda = 3.55$–3.85 μm (Fig. 2b). No evidence for other significant emission lines, including OH prompt emission, could be identified in this spectral region. A possible weak line of H_2CO could be present at 3.689 μm, just to the red of the 3.692 μm HDO line, but H_2CO contamination of the HDO signal is expected to be negligible, considering that the expected (stronger) H_2CO lines between 3.58–3.61 μm are not readily apparent in our data. Due to a relatively complex continuum shape in this region, a 7th-order polynomial was required to obtain a good fit to the baseline. The HDO rotational temperature within a $d = 3''$ circular aperture (16 ± 3 K) was found to be consistent with that of H_2O at 2.7 μm, which justifies the application of the $T_{rot}(\rho)(H_2O;\ 2.7\ \mu m)$ values during the HDO fitting. Taking the average of the outer 5 annuli of the Q-curve (Extended Data Fig. 1a) results in $Q_t(\text{HDO}) = (3.20 \pm 0.19) \times 10^{25}$ s^{-1}. This corresponds to $Q_t(\text{HDO})/Q_t(H_2O) = (1.95 \pm 0.13) \times 10^{-2}$, or D/H = (0.98 ± 0.06)% (taking into account the number of hydrogen atoms in H_2O).

To determine $Q_\rho(CO_2)$ and $T_{rot}(\rho)(CO_2)$, the continuum-subtracted NIRSpec data cube was simultaneously fit for CO_2 and $^{13}CO_2$ components in the range 4.15–4.50 μm. These values were then held fixed to derive $Q_\rho(^{13}CO_2)$ using the non-continuum-subtracted cube (confined within the spectral range 4.34–4.50 μm), but this time including a variable polynomial baseline in the PSG retrieval. Continuum definition is nontrivial in the vicinity of the $^{13}CO_2$ band due to the presence of a relatively broad, unidentified spectral feature on the long-wavelength side of the $^{13}CO_2$ P-branch (around 4.42 μm), combined with the close proximity of the main CO_2 band on the short-wavelength side of the Q-branch, for which the high-J lines are not accurately modelled. We therefore investigated the effects of continuum uncertainty on $Q_t(^{13}CO_2)$ by generating an ensemble of Q-curve fits, each with a different polynomial baseline order (between 1–5). Due to potential contamination of the $^{13}CO_2$ P-branch by the aforementioned unidentified spectral feature, we also performed a separate ensemble

ACCELERATED ARTICLE PREVIEW

of fits, masking the region between λ = 4.380–4.445 μm (to exclude the $^{13}CO_2$ P-branch as well as the unidentified feature). The resulting range of fitted baselines is shown in Extended Data Fig. 3a. The corresponding $Q_t(^{13}CO_2)$ values (and associated $^{12}C/^{13}C$ ratios) for each of the fitted baselines are shown in Extended Data Table 2, along with the reduced χ^2 values (χ^2_R) for the (model minus fit) residuals. From the best-fitting $Q_t(CO_2)$ value of $(1.76 \pm 0.01) \times 10^{27}$ s^{-1} combined with the range of possible $Q_t(^{13}CO_2)$ values, we derive $Q_t(CO_2)/Q_t(^{13}CO_2)$ = 141–191 (including the 1σ statistical error margins on each retrieved measurement).

The region between λ = 4.5–5.1 μm contains the strong $v = 1 - 0$ band of CO, in addition to a blend of ^{13}CO, H_2O, CN and OCS emission features. Retrieving the $^{12}CO/^{13}CO$ ratio therefore requires careful modelling of all these features. All gases were modelled as parent species apart from CN, for which the parent scale length was taken from ref. [58]. We performed a Q-curve analysis for CO by fitting the production rates for all species as a function of ρ, in addition to retrieving $T_{rot}(\rho)$(CO) (see Extended Data Figs. 1c and 5), with a 5th-order polynomial baseline included in the PSG fit. The resulting terminal production rate was $Q_t(CO) = (3.94 \pm 0.01) \times 10^{27}$ s^{-1}. The fit to the CO $v = 1 - 0$ band is very good apart from in the highest-J CO lines, some of which are blended with lines of ^{13}CO (Fig. 2e). Therefore, to retrieve $Q_\rho(^{13}CO)$, we focused on the λ = 4.71–5.05 μm region (which contains 15 individual lines of ^{13}CO), with the poorly-fitting higher-J CO lines masked out so that those regions did not influence the fit (see Fig. 2f). We performed the Q-curve analysis for ^{13}CO by fixing the rotational temperatures according to the previously retrieved $T_{rot}(\rho)$(CO) curve, with polynomial baseline orders between 1–5; in each case, the polynomial coefficients were optimised during fitting so that their uncertainties propagated into the final error estimates on $Q_\rho(^{13}CO)$. The resulting range of fitted baselines is shown in Extended Data Fig. 3b. Due to the weakness of the lines, the ^{13}CO signal became too noisy toward the edge of the field of view, so the last two annuli were omitted from the ^{13}CO Q-curve analysis (Extended Data Fig. 1c). The best-fitting $Q_t(^{13}CO)$ value and associated $^{12}C/^{13}C$ ratio and χ^2_R for each baseline order is given in Extended Data Table 3, corresponding to a range of $^{12}CO/^{13}CO$ values between 123–172 (including 1σ statistical error margins).

Taking the average of the last 5 points in the Q-curves for CN and OCS, from our fits to the λ = 4.5–5.1 μm region, the resulting Q_t(CN) and Q_t(OCS) values for each baseline order are given in Extended Data Table 3. Averaged over the set of 5 different baseline orders, we derive $Q_t(CN) = (3.10 \pm 0.6) \times 10^{24}$ s^{-1} and $Q_t(OCS) = (4.70 \pm 0.49) \times 10^{24}$ s^{-1}, where the errors are the average statistical uncertainties combined in quadrature with the standard deviations of the respective Q_t values (across the 5 different baseline orders). Q_t(CN) should be considered a strict lower limit because CN is produced in the comae of Solar System comets with a radial scale length $\sim 3\times10^4$ km [59], so the majority of its production is expected to occur outside of the NIRSpec field of view.

The measured OCS/CO_2 production rate ratio is (0.27 ± 0.03)%. This is significantly less than the values of 0.6–0.9% found in comet 67P/Churyumov-Gerasimenko [60], and may indicate a relatively low elemental S/O value for the 3I/ATLAS originating system.

ACCELERATED ARTICLE PREVIEW

ALMA Observations

Submillimeter interferometric observations of comet 3I/ATLAS were obtained with the Atacama Compact Array (ACA) sub-component of the Atacama Large Millimeter/submillimeter Array (ALMA) as part of ALMA project 2025.A.00004.S. The observations were conducted in nominal Band 7 weather conditions on 2025-Dec-22 between UT 07:32–08:36, using 11×7 m antennas, with a median zenith precipitable water vapour column of 0.33 mm. The Band 7 receiver was configured to simultaneously observe the CO $J = 3 - 2$ line at 345795.990 MHz at a spectral resolution of 122 kHz and the HCN $J = 4 - 3$ line at 354505.477 MHz at a spectral resolution of 61 kHz. The position and radial velocity of the object were tracked using JPL Horizons solution #44. The interferometric data were flagged and calibrated in the Common Astronomy Software Applications (CASA) package [61] using standard scripts supplied by the Joint ALMA Observatory. The interferometric point-spread function was then deconvolved from the spectral image data using the CASA `tclean` Hogböm algorithm with natural weighting, using a mask size equal to the primary beam FWHM and stopping at a threshold of twice the RMS noise. The resulting (2D Gaussian) beam FWHM was $5.08'' \times 3.37''$ for CO and $4.91'' \times 3.28''$ for HCN.

The molecular spectra were extracted from the CO and HCN integrated emission peak position, then subjected to modelling using the SUBLIME radiative transfer code [62], in order to derive the gas outflow velocities (v_{out}). The latest theoretical state-to-state collisional rates were used for H_2O–CO [63] and H_2O–CN [64], with photolysis rates for the active Sun [56] and solar pumping rates from refs. [62, 65]. For the HCN $J = 4 - 3$ line, hyperfine components were included as described by Cordiner et al. [66]. Our calculations assumed $Q_t(H_2O) = 1.7 \times 10^{27}$ s^{-1} and $T_{kin} = 40$ K (based on $T_{rot} = 40.3 \pm 0.3$ K retrieved from our JWST CO data within a $d = 3''$ circular aperture). Ideally, collisions with CO and CO_2 should also be considered in the SUBLIME molecular excitation calculation, but in reality, the retrieved outflow velocities are not affected by the assumed collision rates. Because the gas coma of 3I/ATLAS is larger than the maximum recoverable scale for the ACA ($\sim 19''$), interferometric flux losses were modelled by applying a constant flux loss factor of 0.75 for the central beam, which was derived by comparing the peak flux of our model CO image before and after processing it using the CASA `simobserve` task.

Assuming a spherically-symmetric coma, the best-fitting SUBLIME models gave $v_{out}(\mathrm{CO}) = 0.345 \pm 0.010$ km s^{-1}; $Q(\mathrm{CO}) = (2.64 \pm 0.01) \times 10^{27}$ s^{-1}, and $v_{out}(\mathrm{HCN}) = 0.276 \pm 0.015$ km s^{-1}; $Q(\mathrm{HCN}) = (6.75 \pm 0.54) \times 10^{24}$ s^{-1} (see Extended Data Fig. 2). These gas outflow velocities are smaller than the values ~ 0.5 km s^{-1} typically found in comets at similar heliocentric distances, which can be explained as a result of outgassing driven by a species with a higher molecular weight than H_2O [3]. This is consistent with the high CO_2/H_2O and CO/H_2O abundances (greater than unity) measured in 3I/ATLAS by JWST and ALMA, implying that CO and CO_2 sublimation are the main drivers of outgassing in this comet. Since the region of the coma where the gases are accelerated (close to the nucleus) is typically in collisional equilibrium [67], different molecules are expected to share a common outflow velocity. Differences could occur as a result of angular variations in the coma composition, or a different balance of production rates from nucleus *vs.* icy grain sublimation for different species.

ACCEPTED ARTICLE PREVIEW

Therefore, to model our JWST CO_2 and H_2O data (for which spectrally resolved line profiles were not available), we take the average of the CO and HCN outflow velocities: $v_{out} = 0.310$ km s^{-1}, while the observed value of $v_{out} = 0.345$ km s^{-1} was used for CO. Ultimately, the use of the Q-curve formalism for deriving isotopic ratios helps minimize optical depth effects, such that uncertainties in v_{out} have a linear effect on our presented absolute molecular production rates. Consequently, v_{out} uncertainties should have negligible impact on the retrieved isotopic ratios.

Methods References

[49] Böker T, Arribas S, Lützgendorf N, Alves de Oliveira C, Beck TL, Birkmann S, et al. The Near-Infrared Spectrograph (NIRSpec) on the James Webb Space Telescope. III. Integral-field spectroscopy. Astron. Astrophys.. 2022 May;661:A82. https://doi.org/10.1051/0004-6361/202142589. arXiv:2202.03308. [astro-ph.IM].

[50] Bushouse H, Eisenhamer J, Dencheva N, Davies J, Greenfield P, Morrison J, et al.: JWST Calibration Pipeline. Zenodo. Available from: https://doi.org/10.5281/zenodo.16280965.

[51] Law DR, E Morrison J, Argyriou I, Patapis P, Álvarez-Márquez J, Labiano A, et al. A 3D Drizzle Algorithm for JWST and Practical Application to the MIRI Medium Resolution Spectrometer. Astron. J.. 2023 Aug;166(2):45. https://doi.org/10.3847/1538-3881/acdddc. arXiv:2306.05520. [astro-ph.IM].

[52] Tholen DJ, Chesley SR. Groundbased Ephemeris Development Effort for Star-Dust Target Wild 2. In: AAS/Division for Planetary Sciences Meeting Abstracts #36. vol. 36 of AAS/Division for Planetary Sciences Meeting Abstracts; 2004. p. 34.16.

[53] Farnocchia D, Bellerose J, Bhaskaran S, Micheli M, Weryk R. High-fidelity comet 67P ephemeris and predictions based on Rosetta data. Icarus. 2021 Apr;358:114276. https://doi.org/10.1016/j.icarus.2020.114276.

[54] Villanueva G, Liuzzi G, Faggi S, Protopapa S, Kofman V, Fauchez TJ, et al. Radiative Transfer Modeling. In: Fundamentals of the Planetary Spectrum Generator 2025 Edition. vol. 1; 2025. p. 43–63.

[55] Woodward CE, Bockélee-Morvan D, Harker DE, Kelley MSP, Roth NX, Wooden DH, et al. A JWST Study of the Remarkable Oort Cloud Comet C/2017 K2 (PanSTARRS). Planet. Sci. J.. 2025 Jun;6(6):139. https://doi.org/10.3847/PSJ/add1d5. arXiv:2504.19849. [astro-ph.EP].

[56] Huebner WF, Mukherjee J. Photoionization and photodissociation rates in solar and blackbody radiation fields. Planet. Space Sci.. 2015 Feb;106:11–45. https://doi.org/10.1016/j.pss.2014.11.022.

ACCELERATED ARTICLE PREVIEW

[57] Mumma MJ, Weaver HA, Larson HP. The Ortho-Para Ratio of Water Vapor in Comet p/ Halley. Astron. Astrophys.. 1987 Nov;187:419.

[58] A'Hearn MF, Millis RC, Schleicher DO, Osip DJ, Birch PV. The ensemble properties of comets: Results from narrowband photometry of 85 comets, 1976-1992. Icarus. 1995 Dec;118(2):223–270. https://doi.org/10.1006/icar.1995.1190.

[59] Fray N, Bénilan Y, Cottin H, Gazeau MC, Crovisier J. The origin of the CN radical in comets: A review from observations and models. Planet. Space Sci.. 2005 Oct;53(12):1243–1262. https://doi.org/10.1016/j.pss.2005.06.005.

[60] Bockelée-Morvan D, Crovisier J, Erard S, Capaccioni F, Leyrat C, Filacchione G, et al. Evolution of CO_2, CH_4, and OCS abundances relative to H_2O in the coma of comet 67P around perihelion from Rosetta/VIRTIS-H observations. Mon. Not. R. Astron. Soc.. 2016 Nov;462:S170–S183. https://doi.org/10.1093/mnras/stw2428. arXiv:1609.07252. [astro-ph.EP].

[61] CASA Team, Bean B, Bhatnagar S, Castro S, Donovan Meyer J, Emonts B, et al. CASA, the Common Astronomy Software Applications for Radio Astronomy. Publ. Astron. Soc. Pac.. 2022 Nov;134(1041):114501. https://doi.org/10.1088/1538-3873/ac9642. arXiv:2210.02276. [astro-ph.IM].

[62] Cordiner MA, Coulson IM, Garcia-Berrios E, Qi C, Lique F, Zołtowski M, et al. A SUBLIME 3D Model for Cometary Coma Emission: The Hypervolatile-rich Comet C/2016 R2 (PanSTARRS). Astrophys. J.. 2022 Apr;929(1):38. https://doi.org/10.3847/1538-4357/ac5893. arXiv:2202.11849. [astro-ph.EP].

[63] Faure A, Lique F, Loreau J. The effect of CO-H_2O collisions in the rotational excitation of cometary CO. Mon. Not. R. Astron. Soc.. 2020 Mar;493(1):776–782. https://doi.org/10.1093/mnras/staa242. arXiv:2001.09562. [astro-ph.EP].

[64] Żółtowski M, Lique F, Żuchowski P, Kłos J, Loreau J, Kedziera D. Collisional excitation of HCN by H_2O. Mon. Not. R. Astron. Soc.. 2025 Jun;540(1):626–632. https://doi.org/10.1093/mnras/staf477.

[65] Cordiner MA, Roth NX, Milam SN, Villanueva GL, Bockelée-Morvan D, Remijan AJ, et al. Gas Sources from the Coma and Nucleus of Comet 46P/Wirtanen Observed Using ALMA. Astrophys. J.. 2023 Aug;953(1):59. https://doi.org/10.3847/1538-4357/ace0bc. arXiv:2305.04822. [astro-ph.EP].

[66] Cordiner MA, Darnell K, Bockelée-Morvan D, Roth NX, Biver N, Milam SN, et al. Evidence for Surprising Heavy Nitrogen Isotopic Enrichment in Comet 46P/Wirtanen's Hydrogen Cyanide. Planet. Sci. J.. 2024 Oct;5(10):221. https://doi.org/10.3847/PSJ/ad7829. arXiv:2409.05711. [astro-ph.EP].

[67] Zakharov VV, Rotundi A, Bockelée-Morvan D, Bykov NY, Fulle M, Biver N, et al. Stationary expansion of gas mixture from a spherical source into vacuum.

ACCELERATED ARTICLE PREVIEW

Icarus. 2023 May;395:115453. https://doi.org/10.1016/j.icarus.2023.115453.

[68] Roth NX.: jwstComet: A spectral analysis package for Python. Zenodo.

Acknowledgements. This work is based on observations made with the NASA/ESA/CSA James Webb Space Telescope. The data were obtained from the Mikulski Archive for Space Telescopes at the Space Telescope Science Institute, which is operated by the Association of Universities for Research in Astronomy, Inc., under NASA contract NAS 5-03127 for JWST. We acknowledge Matthew Hopkins for input on the Galactic (dynamical) origin of 3I/ATLAS. We gratefully acknowledge the assistance of optical observers who submitted astrometric observations of 3I/ATLAS in the weeks leading up to our observations, to help refine the ephemeris position. In particular, we thank J. Chatelain, , M. Frissell, E. Gomez, S. Greenstreet, W. Hoogendam, C. Holt, K. Meech, H. W. Lin, T. Lister, L. Salazar Manzano, T. Santana-Ros, D. Seligman, D. Singh, Q. Ye, Q. Zhang. Supporting astrometric observations were obtained by the Comet Chasers school outreach program (https://www.cometchasers.org/), led by Helen Usher, which is funded by the UK Science and Technology Facilities Council (via the DeepSpace2DeepImpact Project), the Open University and Cardiff University. It accesses the LCOGT telescopes through the Schools Observatory/Faulkes Telescope Project (TSO2025A-00 DFET-The Schools' Observatory), which is partly funded by the Dill Faulkes Educational Trust, and through the LCO Global Sky Partners Programme (LCOEPO2023B-013). Observers included individuals and representatives from the following schools and clubs: E. Maciulis, A. Bankole, J. Bower, O. Roberts, participants on the British Astronomical Associations' Work Experience project 2025 from The Coopers Company & Coborn School, Upminster, UK; St Marys Catholic Primary School, Bridgend, UK; J. M. Perez Redondo & Students: A. Matea, L. Guillamet, A. Montoy, and A. Martin from Institut d'Alcarràs, Catalonia, Spain; Louis Cruis Astronomy Club, Brazil; Jelkovec High School, Zagreb, Croatia, and C. Wells at a British Astronomical Association event. ALMA is a partnership of ESO, NSF (USA), NINS (Japan), NRC (Canada), NSC and ASIAA (Taiwan) and KASI (Republic of Korea), in cooperation with the Republic of Chile. The JAO is operated by ESO, AUI/NRAO and NAOJ. The NRAO is a facility of the National Science Foundation operated under cooperative agreement by Associated Universities, Inc.. This research has made use of NASA's Astrophysics Data System Bibliographic Services. This research has made use of data and/or services provided by the International Astronomical Union's Minor Planet Center.

- **Data Availability:** All JWST data are available through the Mikulski Archive for Space Telescopes at the Space Telescope Science Institute under proposal ID #5094 (https://doi.org/10.17909/1jvn-1z72). This work makes use of ALMA data set ADS/JAO.ALMA#2025.A.00004.S, which is available for download from the ALMA Science Archive (http://almascience.nrao.edu/aq/). All scripts and data required to reproduce the results of this study are available for download from Zeonodo (https://doi.org/10.5281/zenodo.20531681 and https://doi.org/10.5281/zenodo.20531500)

ACCELERATED ARTICLE PREVIEW

- **Code Availability:** The JWST Calibration Pipeline software [50] is available from https://github.com/spacetelescope/jwst.
  The Planetary Spectrum Generator [15], used for modelling cometary infrared emission lines is available at https://psg.gsfc.nasa.gov/.
  The `jwstComet` software [68], used for extracting spectra from JWST data cubes and modelling them with PSG, is available from https://github.com/apertureSynthesis/jwstComet.
  The 1D version of the SUBLIME radiative transfer code [62], used for modelling the ALMA data, is available from https://github.com/mcordiner/sublime-d1dc. The `sublimed1dFit` code for generating optimised spectral line models using SUBLIME is available from https://github.com/mcordiner/sublimed1dFit.
- **Author Contributions:** M.A.C calibrated the JWST and ALMA data, performed the NIRSpec G395H spectral extraction and modelling, and led the manuscript writing. N.X.R. and G.V. contributed to the data analysis methodology, performed the G235H (2.7 μm) H_2O band modelling, and independently checked the isotopic ratio retrievals. C.O.C. obtained astrometric images using the APO. M.M. performed astrometric measurements. D.F. calculated the 3I/ATLAS orbit and ephemeris. S.B.C. helped interpret the isotopic ratios. N.B., D.B.-M., D.B., J.C., M.N.D., K.F., M.S.P.K., S.N.M., J.W.N., C.O., M.E.S. and C.A.T. helped with the project design, data acquisition, interpretation of results, and editing of the manuscript.
- **Funding:** M.A.C., N.X.R., S.B.C. and S.N.M. were supported by the NASA Planetary Science Division Internal Scientist Funding Program through the Fundamental Laboratory Research work package (FLaRe). C.O.C. acknowledges support from the DIRAC Institute in the Department of Astronomy at the University of Washington. D.F. conducted this research at the Jet Propulsion Laboratory, California Institute of Technology, under a contract with the National Aeronautics and Space Administration (80NM0018D0004). M.E.S. acknowledges support in part from UK Science and Technology Facilities Council (STFC) grant ST/X001253/1. LINCC Frameworks is supported by Schmidt Sciences.
- **Competing Interests:** The authors declare no competing interests.

ACCELERATED ARTICLE PREVIEW

Fig. 1: **Spectrally integrated line flux maps for 3I/ATLAS observed using JWST NIRSpec.** (a) H_2O at 2.7 μm, (b) CO_2 at 4.3 μm, (c) CO at 4.7 μm. Image axes are aligned with the equatorial (RA/decl.) grid. Molecular emission has been isolated by subtracting a polynomial fit to the adjacent continuum. Spatial coordinates are with respect to the brightest pixel in each map (the pseudo-nucleus). Inset panels (upper right) show the continuum-subtracted spectra within the image integration wavelength range, spatially integrated within a 3″ diameter circular aperture centered on the pseudo-nucleus (corresponding to 3,900 km at the 1.8 au distance of the comet from the telescope). Lower left corner shows the direction of the (sky-projected) comet-Sun (S) and nucleus velocity (v) vectors.

Fig. 2: **Observed NIRSpec molecular spectra of 3I/ATLAS**. Spectra have been integrated within a $d = 3.6''$-diameter circular aperture centered on the pseudo-nucleus. Similarly spatially-integrated, best-fitting spectral models are overlaid, with (observation minus model) residuals in the lower sub-panels. As shown by the grey filled regions in panel (a), the strong CO ($v = 1 - 0$) lines were subtracted prior to fitting, to reduce spectral contamination when fitting H_2O. The grey region in panel (d) indicates wavelengths excluded (masked) from the fitting due to potential contamination by an unidentified feature around 4.42 μm. In panel (f), the regions surrounding the stronger CO lines (shown in grey) were masked during ^{13}CO fitting, to avoid contamination by the CO model residuals, and to allow improved fitting of the higher-J CO lines, some of which overlap ^{13}CO. For panels (d) and (f), 5th-order baseline fits are shown; see Extended Data Fig. 3 for the ensemble of baselines used in deriving our final range of plausible $^{12}C/^{13}C$ values for these species.

Fig. 3: **Galactic and Solar System Isotopic ratios.** Observed isotopic ratio in the coma of 3I/ATLAS compared with Galactic and Solar System observations for (a) D/H and (b) $^{12}C/^{13}C$. Data are from the compilation of Nomura et al. [12], with additional D/H values for 12P/Pons-Brooks [16], V883 Ori (gas-phase [17]), and IRAS20126+4104, HOPS370 and L1527 (ice-phase [18, 19]). D/H data are for H_2O unless otherwise specified. The "disks HCN" data represent the mean and range of observed D/H values across five protoplanetary disks. "MYSOs" data is the mean and range for massive young stellar objects. For $^{12}C/^{13}C$, the range of plausible fit results (including 1σ statistical errors) is given for 3I/ATLAS. The meteoritic "XCO_3" and "IOM" data are the mean values (and ranges) for carbonates and insoluble organic matter, respectively, in carbonaceous chondrites [20–22]. We also plot TW Hya and HD 163296 CO isotopic ratios [23, 24], mean protostellar ice CO and CO_2 values [25], protostellar CO gas (mean and range) [26], interstellar CO_2 ice (mean and range) [27], interstellar HCO^+ isotopic ratios for two Galactocentric distances (r_G) [28], $r_G = 14$ kpc CN data [29], super-Jupiter exoplanet CO data [30], and M dwarf GJ745 data [31]. Error bars are 1σ unless otherwise specified.

ACCELERATED ARTICLE PREVIEW

Extended Data Figure 1: **Measured production rate (Q) curves.** Best fitting production rates for (a) H_2O, (b) CO_2, and (c) CO, and their respective minor isotopologues, as a function of sky-projected distance from the nucleus (ρ). Spectra were extracted and modelled within successive $0.2''$-thick annuli centered on the coma flux peak to generate Q_ρ. For $^{13}CO_2$ and ^{13}CO, the models included a 5th-order polynomial baseline fit. Vertical error bars indicate 1σ statistical uncertainties, while the horizontal error bars indicate the radial extent of each spatial region.

Extended Data Figure 2: **3I/ATLAS ALMA spectra.** High-resolution submillimeter-wave spectra of (a) CO and (b) HCN line emission from 3I/ATLAS, observed using the ALMA ACA on 2025-Dec-22. Spectra were extracted at the common emission peak for both species, and are plotted on a velocity scale with respect to the rest frequencies of the CO $J = 3 - 2$ and HCN $J = 4 - 3$ lines, respectively. Best fitting spectral models are overlaid, consistent with an average terminal H_2O OPR of 2.74 ± 0.03.

Extended Data Figure 3: **3I/ATLAS JWST spectra with a range of baseline fits.** Spectra observed in the vicinity of (a) the $^{13}CO_2$ ν_3 band and (b) the ^{13}CO $v = 1 - 0$ band, integrated within a $d = 3.6''$ circular aperture. The ensemble of best-fitting polynomial baselines considered as part of our spectral modelling is overlaid, corresponding to the $Q_t(^{13}CO_2)$ and $Q_t(^{13}CO)$ values shown in Extended Data Tables 2 and 3, respectively. For those fits labeled 'm' in panel (a), the potentially contaminated region between $\lambda = 4.380$–4.445 μm (highlighted in grey) was excluded (masked) during fitting. For both panels, the "total model" curves are for the minimum χ^2_R model (using a 5th order baseline in both cases). For ^{13}CO, numerous emission lines from additional species are present (see Fig. 2f for details).

Extended Data Figure 4: **3I/ATLAS JWST H_2O 2.7 μm spectral fit.** NIRSpec observations from 2025-Dec-22, extracted inside a $d = 3.0''$ circular aperture, with independent ortho- and para-H_2O spectral fits overlaid.

Extended Data Figure 5: **Best-fitting molecular rotational temperatures (T_{rot}) as a function of ρ.** Rotational temperatures were retrieved independently for each gas as a function of sky-projected distance from the nucleus (ρ). Vertical error bars indicate 1σ statistical uncertainties, while the horizontal error bars indicate the radial extent of each spatial region.

ACCELERATED ARTICLE PREVIEW

Extended Data Table 1: 3I/ATLAS Observed Gas Production Rates

Extended Data Table 2: $^{13}CO_2$ terminal gas production rates and $^{12}CO_2/^{13}CO_2$ ratios for different baseline fit orders

Extended Data Table 3: $^{12}CO/^{13}CO$ ratios and ^{13}CO, CN and OCS terminal gas production rates for different baseline fit orders

ACCELERATED ARTICLE PREVIEW

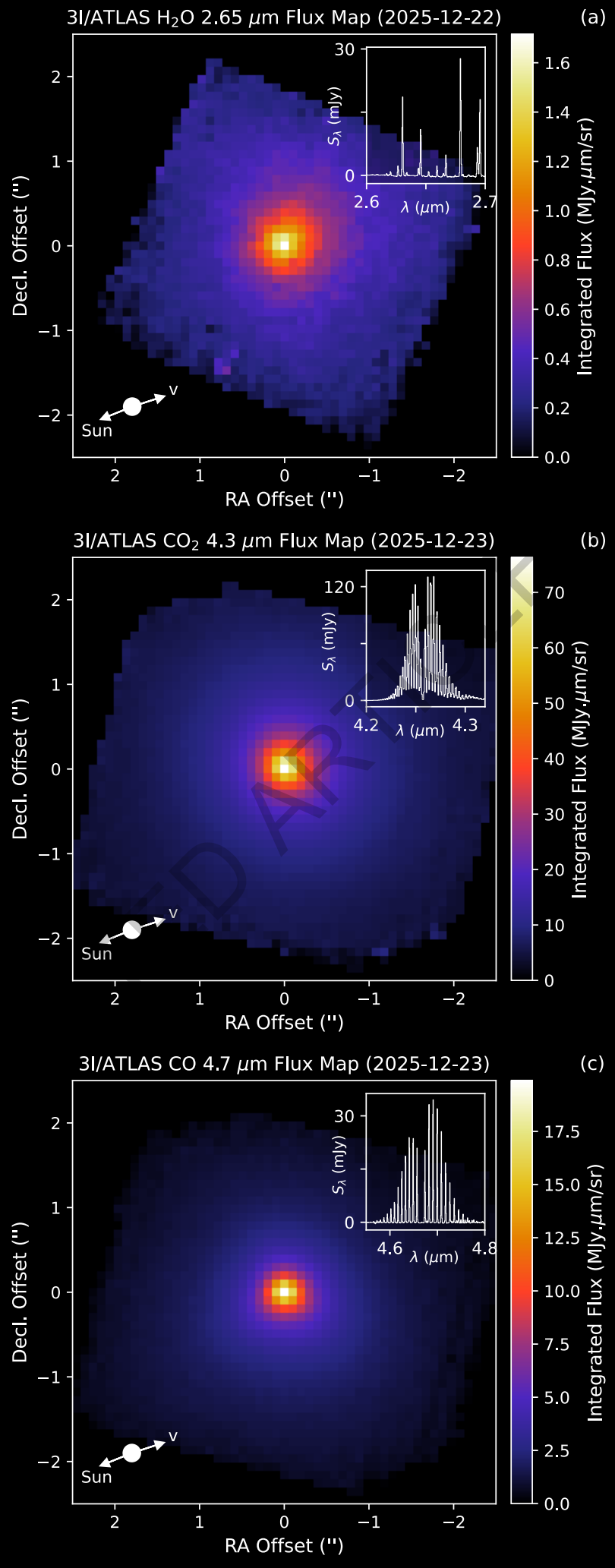
3I/ATLAS H_2O 2.65 μm Flux Map (2025-12-22)
(a)
Decl. Offset ('')
RA Offset ('')
Integrated Flux (MJy.μm/sr)
S_λ (mJy)
λ (μm)
Sun
v
3I/ATLAS CO_2 4.3 μm Flux Map (2025-12-23)
(b)
Decl. Offset ('')
RA Offset ('')
Integrated Flux (MJy.μm/sr)
S_λ (mJy)
λ (μm)
Sun
v
3I/ATLAS CO 4.7 μm Flux Map (2025-12-23)
(c)
Decl. Offset ('')
RA Offset ('')
Integrated Flux (MJy.μm/sr)
S_λ (mJy)
λ (μm)
Sun
v

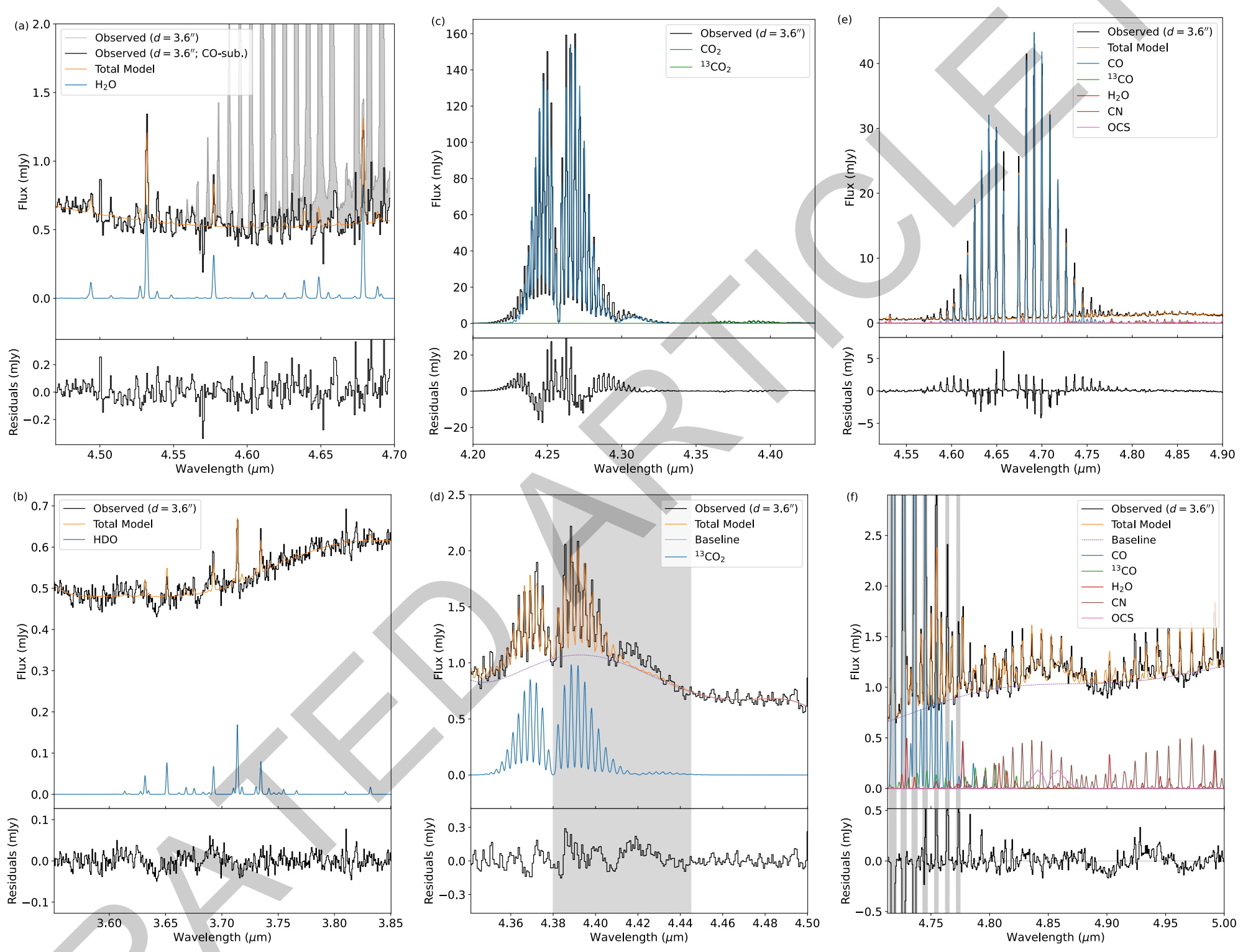

ACCEPTED ARTICLE

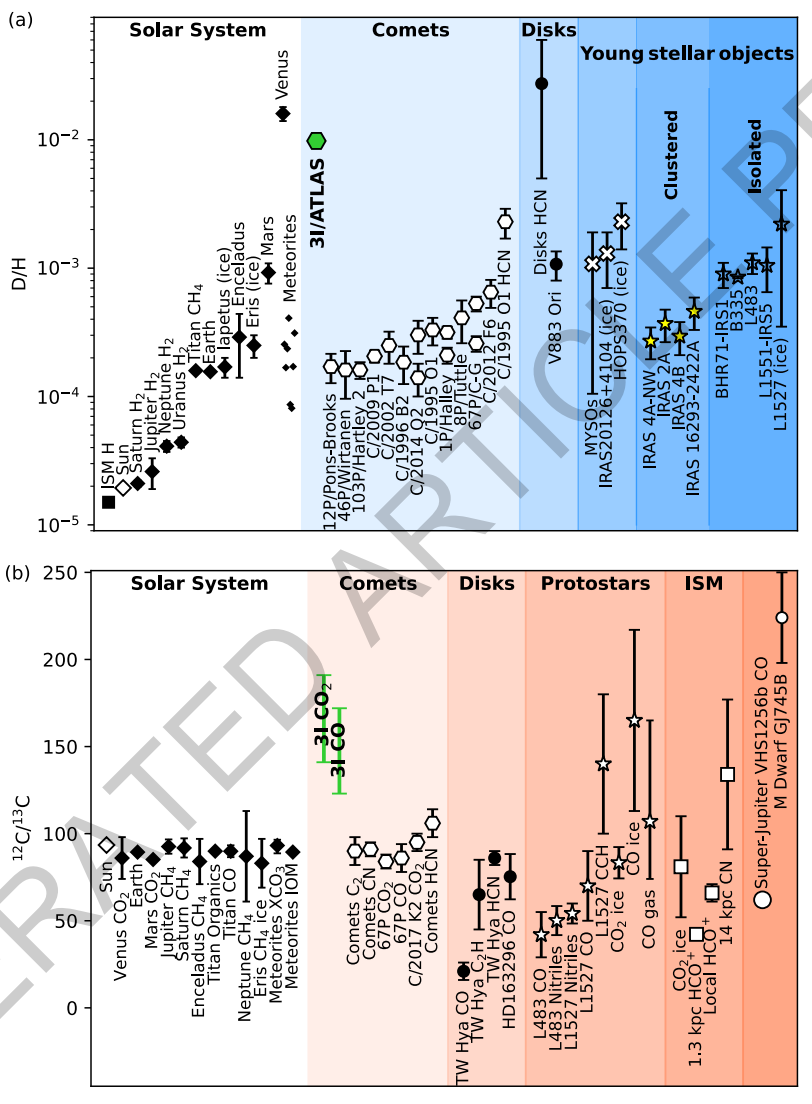

ERATED ARTICLE

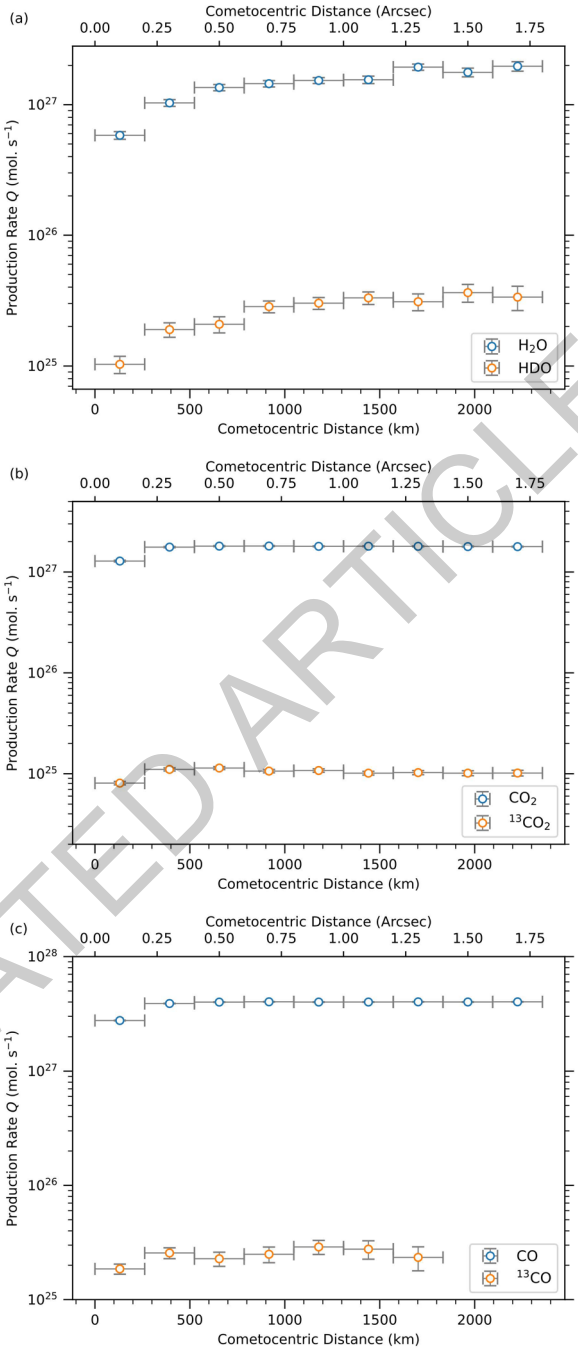

Extended Data Fig. 1

ACCELERATED ARTICLE PREVIEW

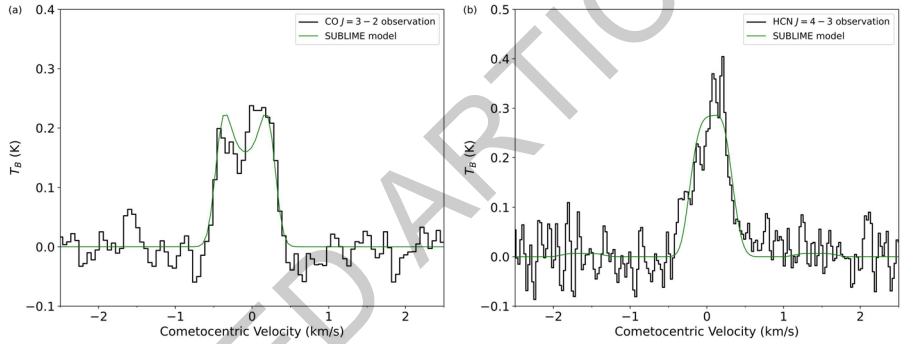

Extended Data Fig. 2

ACCELERATED ARTICLE PREVIEW

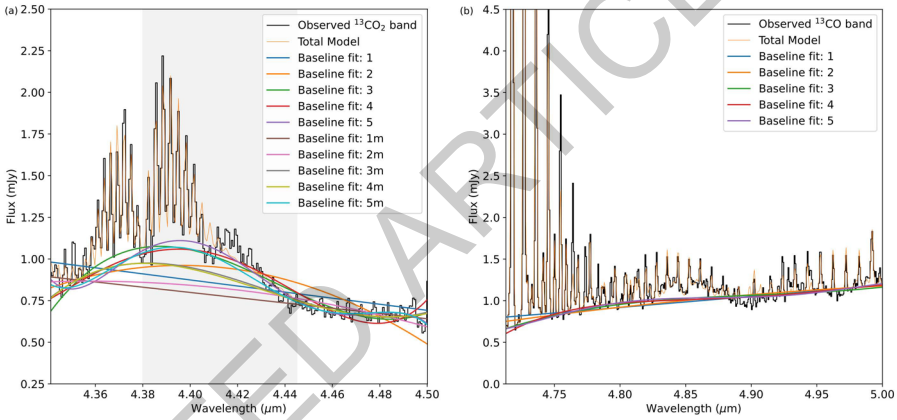

Extended Data Fig. 3

ACCELERATED ARTICLE PREVIEW

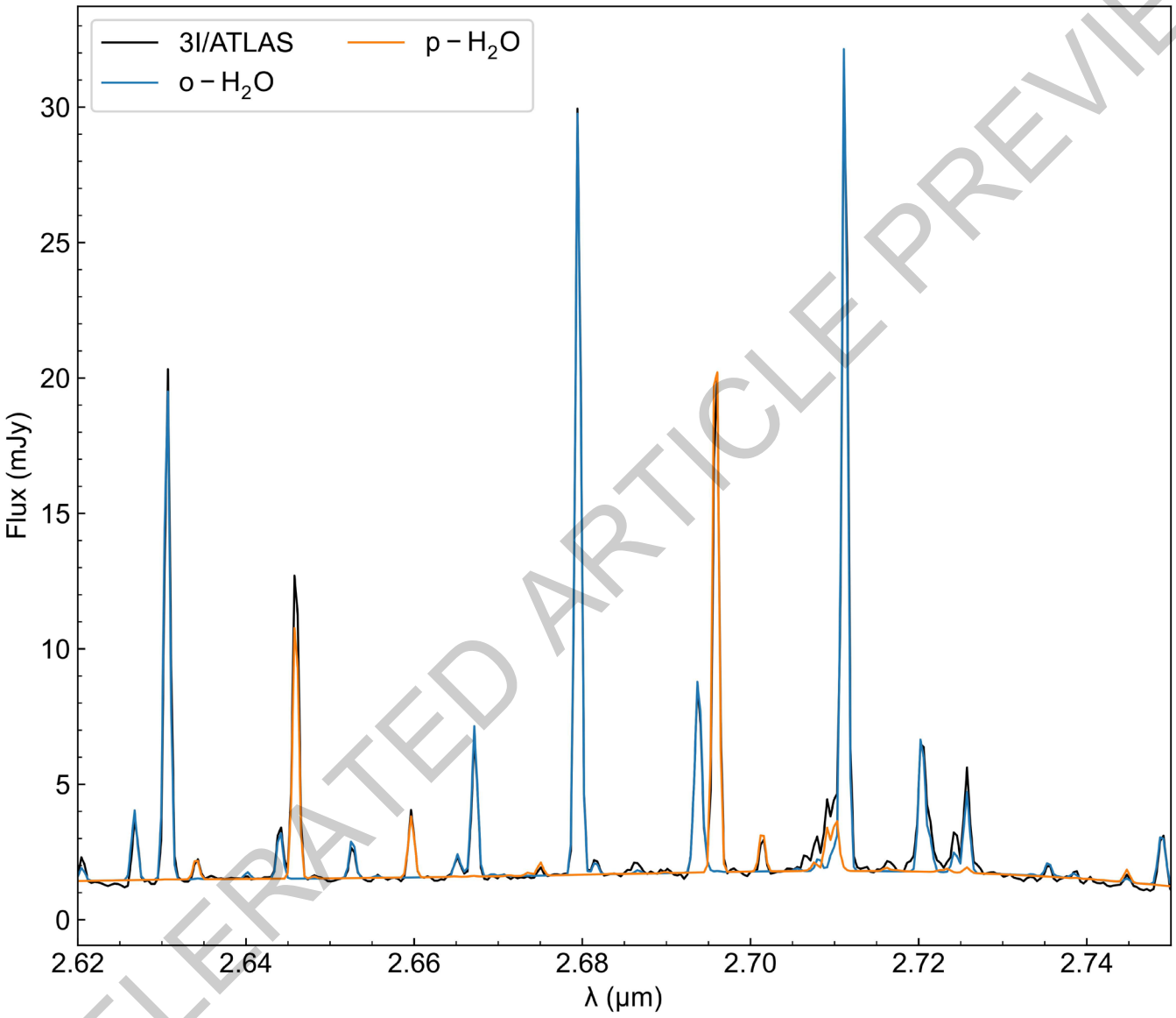

Extended Data Fig. 4

ACCELERATED ARTICLE PREVIEW

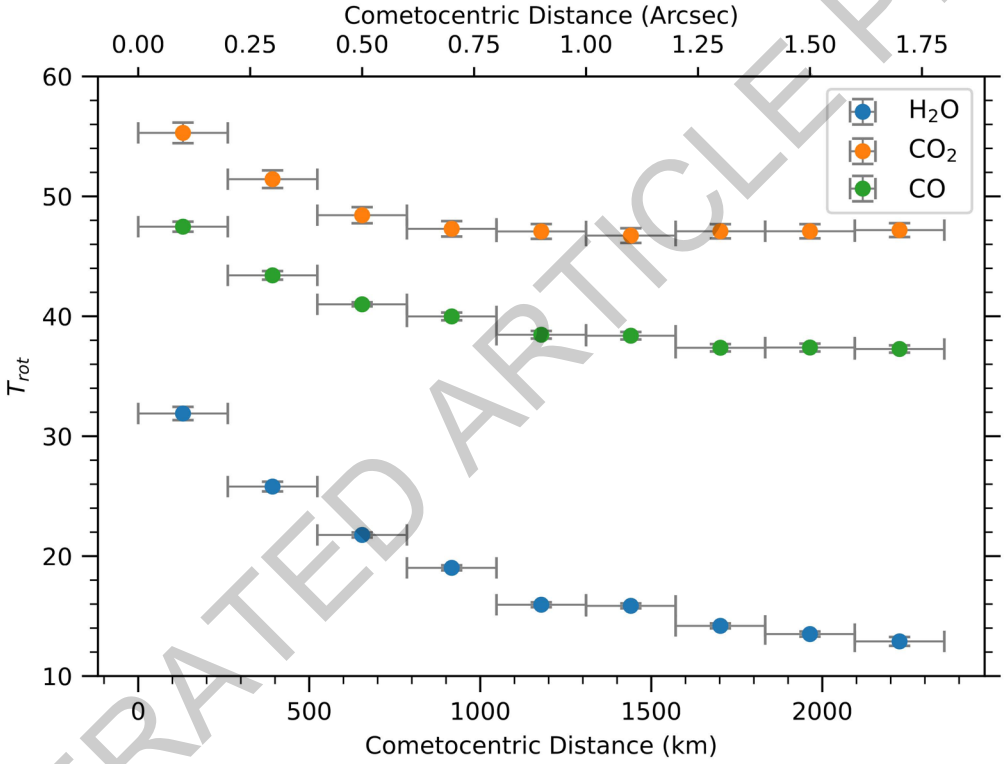

Extended Data Fig. 5

ACCELERATED ARTICLE PREVIEW

Extended Data Table 1: 3I/ATLAS Observed Gas Production Rates

Gas	Band ID	Wavelength (μ)	Q_t (10^{25} s^{-1})
H_2O	$\nu_1 + \nu_3$	2.7	142 ± 1
H_2O	Hot bands	4.6	164 ± 5
HDO	ν_1	3.6	3.20 ± 0.19
CO_2	ν_3	4.3	176 ± 1
$^{13}CO_2$	ν_3	4.4	0.94–1.22
CO	$v = 1$–0	4.7	394 ± 1
^{13}CO	$v = 1$–0	4.8	2.49–2.99
OCS	ν_3	4.9	0.47 ± 0.05
CN	$v = 1$–0	4.9	> 0.31

Notes — Gas production rates (Q_t) in molecules per second, are averaged between $\rho = 0.8$–$1.8''$ to mitigate opacity effects from the inner coma, apart from ^{13}CO, which was averaged between $\rho = 0.4$–$1.4''$ due to its weaker lines (see Methods). Errors on Q_t are the 1σ statistical model-fitting uncertainties. For ^{13}CO and $^{13}CO_2$, the Q_t ranges correspond to the ensemble of best-fitting values across a range of plausible baseline models, and include the (additive) statistical uncertainties.

Extended Data Table 1

ACCELERATED ARTICLE PREVIEW

Extended Data Table 2: $^{13}CO_2$ terminal gas production rates and $^{12}CO_2/^{13}CO_2$ ratios for different baseline fit orders

Order	$Q_t(^{13}CO_2)$ (10^{25} s^{-1})	χ^2_R	$^{12}C/^{13}C$
1	1.22 ± 0.03	9.956	144 ± 3
2	1.10 ± 0.02	6.847	161 ± 3
3	1.15 ± 0.02	4.228	154 ± 3
4	1.05 ± 0.02	3.853	168 ± 4
5	1.02 ± 0.02	3.022	172 ± 4
1(m)	1.11 ± 0.02	13.70	158 ± 3
2(m)	1.10 ± 0.02	10.74	161 ± 3
3(m)	0.97 ± 0.02	6.759	182 ± 4
4(m)	0.95 ± 0.02	7.218	186 ± 4
5(m)	0.94 ± 0.02	3.536	187 ± 4

Note — (m) indicates the fit was performed with the $^{13}CO_2$ P-branch masked between $\lambda = 4.380$–4.445 μm to avoid baseline contamination.

Extended Data Table 2

ACCELERATED ARTICLE PREVIEW

Extended Data Table 3: $^{12}CO/^{13}CO$ ratios and ^{13}CO, CN and OCS terminal gas production rates for different baseline fit orders

Order	$Q_t(^{13}CO)$ (10^{25} s^{-1})	Q_t(CN) (10^{24} s^{-1})	Q_t(OCS) (10^{24} s^{-1})	χ^2_R	$^{12}C/^{13}C$
1	2.90 ± 0.22	3.18 ± 0.07	5.36 ± 0.26	1.761	136 ± 10
2	2.99 ± 0.22	3.11 ± 0.07	4.92 ± 0.26	1.702	133 ± 10
3	2.69 ± 0.21	3.12 ± 0.07	4.18 ± 0.26	1.562	147 ± 12
4	2.53 ± 0.21	3.07 ± 0.07	4.72 ± 0.27	1.463	156 ± 13
5	2.49 ± 0.21	3.05 ± 0.07	4.32 ± 0.29	1.426	158 ± 14

Extended Data Table 3

ACCELERATED ARTICLE PREVIEW